OSCAR: A new modular device for the identification and correlation of low energy particles

D. Dell'Aquila [a,b,d,*], I. Lombardo [a,k,**], G. Verde [d,k], M. Vigilante [a,b], G. Ausanio [a,c], A. Ordine [b], M. Miranda [a], M. De Luca [a], R. Alba [j], L. Augey [l], S. Barlini [e,f], E. Bonnet [m], B. Borderie [d], R. Bougault [l], M. Bruno [g], A. Camaiani [e,f], G. Casini [f], A. Chbihi [m], M. Cicerchia [i,h], M. Cinausero [h], D. Fabris [h], Q. Faible [m], L. Francalanza [b], J.D. Frankland [m], L. Grassi [d], F. Gramegna [h], D. Gruyer [f], A.J. Kordyasz [n], T. Kozik [o], R. LaTorre [a,b], N. Le Neindre [l], O. Lopez [l], T. Marchi [h], L. Morelli [g], P. Ottanelli [e,f], M. Parlog [l], G. Pastore [e,f], G. Pasquali [e,f], S. Piantelli [f], D. Santonocito [j], A.A. Stefanini [e,f], G. Tortone [b], S. Valdrè [m], E. Vient [l]

[a] *Dip. di Fisica "Ettore Pancini", Università di Napoli Federico II, 80126 Napoli, Italy*
[b] *INFN-Sezione di Napoli, 80126 Napoli, Italy*
[c] *Istituto SPIN - CNR, 16152, Genova, Italy*
[d] *Institut de Physique Nucléaire, CNRS-IN2P3, Univ. Paris-Sud, Université Paris-Saclay, 91406 Orsay Cedex, France*
[e] *Dip. di Fisica, Università di Firenze, 50019 Sesto Fiorentino (FI), Italy*
[f] *INFN-Sezione di Firenze, 50019 Sesto Fiorentino (FI), Italy*
[g] *INFN-Sezione di Bologna, 40127 Bologna, Italy*
[h] *INFN-Lab. Naz. di Legnaro, 35020 Legnaro (PD), Italy*
[i] *Dip. di Fisica "Galileo Galilei", Università degli Studi di Padova, 35131 Padova, Italy*
[j] *INFN-Lab. Naz. del Sud, 95125 Catania, Italy*
[k] *INFN-Sezione di Catania, 95125 Catania, Italy*
[l] *LPC Caen, Normandie Univ, ENSICAEN, UNICAEN, CNRS/IN2P3, 14000 Caen, France*
[m] *GANIL, CEA/DSM-CNRS/IN2P3, 14076 Caen, France*
[n] *Heavy Ion Laboratory, Warsaw University, Warsaw, Poland*
[o] *Jagiellionian University, Krakow, Poland*

ARTICLE INFO

Keywords:
Modular detectors
Low identification thresholds
Thin silicon detectors
Silicon uniformity
Ion channeling
Isospin dynamics

ABSTRACT

A new modular and high versatility hodoscope, OSCAR, has been developed and characterized. The aim of this hodoscope is to work as an ancillary detector of present large acceptance heavy ion detectors in specific angular regions where low thresholds and high granularities are needed. We discuss the capabilities of OSCAR in the ΔE–E identification of very low energy light particles, providing a precise map of the thickness uniformity of the ΔE (SSSSD, 20 μm) stage and showing how the thickness gradient affects the identification of particles. Energy spectra of light identified particles produced in Ca + Ca collisions at 35 AMeV are used to investigate isospin transport phenomena involving the emission of low energy particles from the *quasi-target* (QT) source in semi-peripheral nuclear collisions. The possibility to explore particle–particle correlations are also discussed.

1. Introduction

In heavy ions collisions at intermediate energies (20–100 MeV/nucleon) we can observe the formation and the disintegration of different nuclear sources whose properties are strongly affected by the initial composition of the two collision partners and by nuclear dynamics. For example, an interesting case is represented by collisions involving nuclei with different N/Z values, where isospin transport phenomena may occur [1–5]. The investigation of these type of phenomena is particularly suited to probe compressed and diluted phases of Asymmetric Nuclear Matter (ANM) and, in particular, to shed light on the symmetry term of the Nuclear Equation of State (EoS) [6–8]. Moreover, the recent development of new facilities for

* Corresponding author at: Dip. di Fisica "Ettore Pancini", Università di Napoli Federico II, 80126 Napoli, Italy.
** Corresponding author at: INFN-Sezione di Catania, 95125, Catania, Italy.
E-mail address: dellaquila@na.infn.it (D. Dell'Aquila).

radioactive beams (like SPES@INFN-LNL [9], SPIRAL2@GANIL [10] or ISOLDE@CERN [11]) has triggered a new interest in the investigation of isospin effects in low energy nuclear reactions, since they manifest themselves more strongly in the case of nuclear collisions involving projectiles (or targets) with exotic N/Z values.

Experimentally, it is important to investigate isospin transport by probing the isospin composition (N/Z) of the quasi-projectile (QP), quasi-target (QT) and mid-velocity (MV) sources [12–14]. This can be accomplished by measuring the isotopic distribution of the corresponding emitted particles and fragments [13], in the hypothesis that they still maintain some memory of the initial composition of the emitting source [13,15].

Typically, the common used strategy to detect such fragments is to use devices characterized by large solid-angle coverage (like INDRA [16–19], FAZIA [20–22], CHIMERA [23–26] + FARCOS [27,28] GARFIELD [29–31], Miniball + LASSA [32–34], HiRA [35] and NIMROD-ISiS [36–40]), in order to obtain the best possible complete reconstruction of fragmentation events as well as particle identification techniques suited for separating light isotopes. However, the detection and identification of fragments emitted by the QT source is still an open problem. Most of the emissions by the QT consist of low energy particles, whose detection requires good energy resolution and very low identification thresholds. Relevant advances have been achieved recently by means of digital pulse-shaping techniques allowing to identify low energy particles that stop in the first silicon layers of ΔE–E telescope [22]. However, when such emissions originate from the QT, the very small range of particle in solid state detectors makes it difficult to use such pulse-shaping methods. In this case, the coupling with ancillary detectors having lower identification thresholds and better granularity, placed a backward angles, can be a good strategy to probe the N/Z ratio of the QT source.

For these reasons we developed a new modular hodoscope, OSCAR (hOdoscope of Silicons for Correlations and Analysis of Reactions), constituted by two detection stages (20 μm Single Sided Silicon Strip Detector (SSSSD) - 300 μm Silicon pads) and characterized by good segmentation and energy resolution. The presence of a thin silicon layer as first stage allows to obtain low identification thresholds, needed for the detection of QT emitted particles.

This article describes the capability of the OSCAR device to study the disintegration products of slow-moving nuclear sources produced in heavy ion collisions (HIC) at intermediate energies. We studied the isotopic (^{4}He/^{3}He, ^{7}Li/^{6}Li) and isobaric (^{3}H/^{3}He, ^{7}Li/^{7}Be) yield ratios in Ca + Ca collisions at 35 MeV/nucleon. In Section 2 we describe the technical features of OSCAR and we report a detailed characterization of the first (thin) silicon detection stage; Section 3 presents results from the data analysis of Ca + Ca collisions at 35 MeV/nucleon and shows an example of reconstruction of in-flight resonance decays by means of invariant mass analyses performed with OSCAR; conclusions and perspectives are finally discussed in Section 4.

2. OSCAR: Features and capabilities

2.1. Detector's layout

OSCAR is conceived to be a modular hodoscope, based on two segmented silicon detection stages. They are optimized to identify, with high resolution, low energy light particles emitted in nuclear reactions. The main features of this detector are the compactness and the high versatility, given by plug-and-play connections and embedded pre-amplifiers, and the low identification thresholds, thanks to use of a thin silicon detector as a first stage followed by 16 independent silicon pads.

More in detail, the first detection stage is a SSSSD (nominally 20 μm thick) type 2M detector manufactured by the *Micron Semiconductor*, operated at a depletion voltage of 2.5 V. On the front side, an aluminum metallization segments the silicon surface into 16 strips, having a pitch of 3.125 mm with an inter-strip of 0.125 mm nominal value. An inspection of the detector at the optical microscope confirms, within a few percent, these nominal values. The rear side is instead constituted by a single surface with a uniform aluminum metallization layer. A detailed investigation of the interface zone between an Al strip and the adjacent inter-strip region has been performed thanks to the use of a non-destructive analysis based on Atomic Force Microscopy (AFM). The height distribution of a ≈ 46×46 μm^2 wide area at the interface is shown in Fig. 1 in a color scale, indicating the relative height distribution in the analyzed region. It evidently appears the presence of a deep canal (blue region), ≈ 10 μm wide, that separates the Al metallization of each strip (yellow region) from the SiO_2 layer of the inter-strip region (light green region). The three dots are due to micro-metric dust grain on the detector surface. The presence of this narrow (≈ 10 μm) and deep (≈ 200 nm from the inter-strip layer average level) canal is attributed to the manufacturing technique of the detector. If we reasonably assume that the bottom of the narrow canal corresponds to the entrance side of the active detection volume, we can give an estimate of about 680±40 nm for the SSSSD dead entrance layer, on the basis of the height distribution histogram of Fig. 2. This value should be compared with similar results obtained, with a different technique, in Ref. [41] for the same kind of detector.

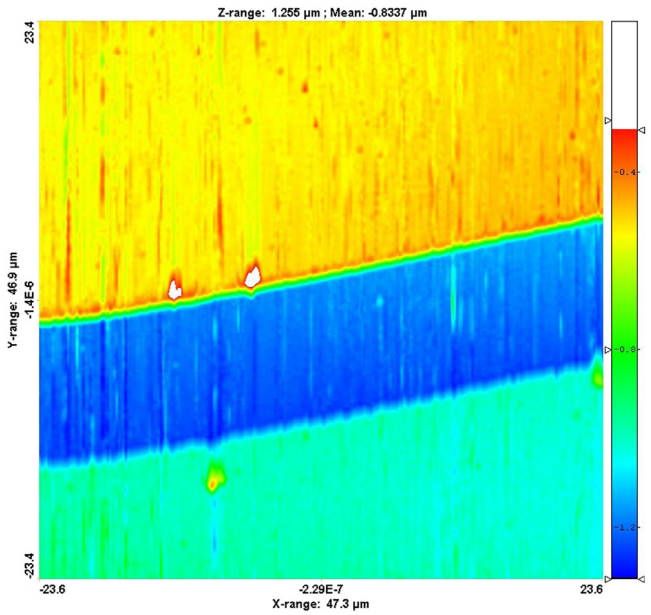

Fig. 1. Atomic Force Microscopy (AFM) profiling of a ≈ 46 × 46 μm^2 area at the interface between an Al strip and the interstrip region. The yellow area corresponds to the Al strip, the green area to the interstrip region. The blue canal is due to the peculiar manufacturing technique of the Si strip detector. The color scale indicate relative heights between the various part of the detector.

A connector collects 16 electric lines from the front side of the detector. These lines are displaced in the ceramic frame to minimize the cross-talk with levels lower than 1%. In the front side they are connected to the active areas of each strip by means of bonds while, in the rear side, only two of them have a bonding connection and the whole surface is maintained to ground. In order to minimize the electronic noise, the strip detector is connected, by means of a short flat cable, with a charge sensitive pre-amplifier model NPA-16FE, manufactured by the *Net Instruments* and installed inside the vacuum chamber. It has a sensitivity of 45 mV/MeV and it was especially designed to work in vacuum, with a low power consumption (< 900 mW) and an aluminum box as heat sink. This compact pre-amplifier works with GND and ±6 V service voltages given via a 5 + 5 pin service connector together with a common bias for the 16 silicon strips. To polarize the silicon we used a bias voltage of 3.0 V, operating in over-depletion regime. In

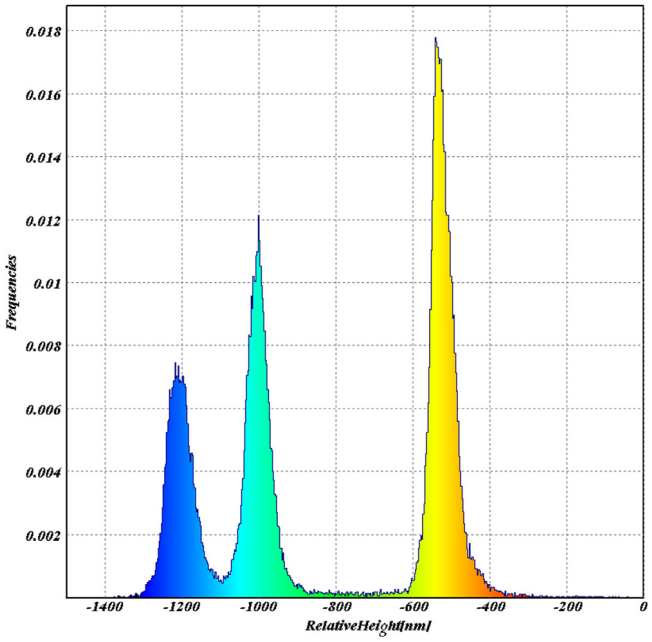

Fig. 2. Frequency histogram of the relative height distribution (in nm) in the region analyzed with the AFM technique. The color scale visually correspond to the three region shown in the bi-dimensional plot. (For interpretation of the references to color in this figure legend, the reader is referred to the web version of this article.)

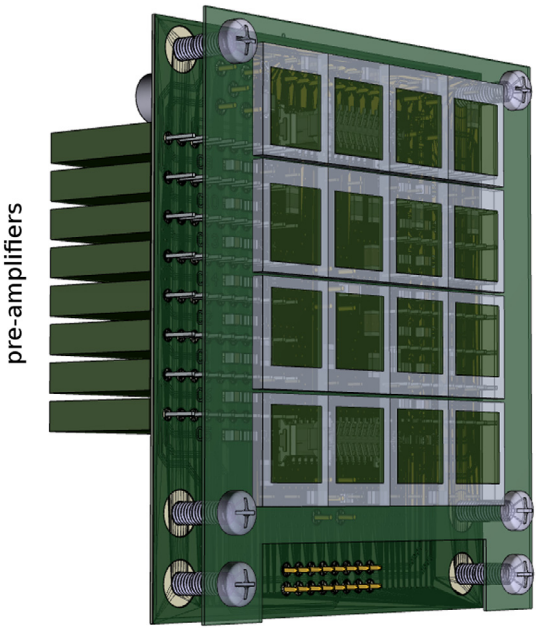

Fig. 3. A schematic view of the second detection stage of OSCAR. The rear board contains two series of 8 compact charge sensitive pre-amplifiers to collect signals from 16 silicon pads welded on the front board.

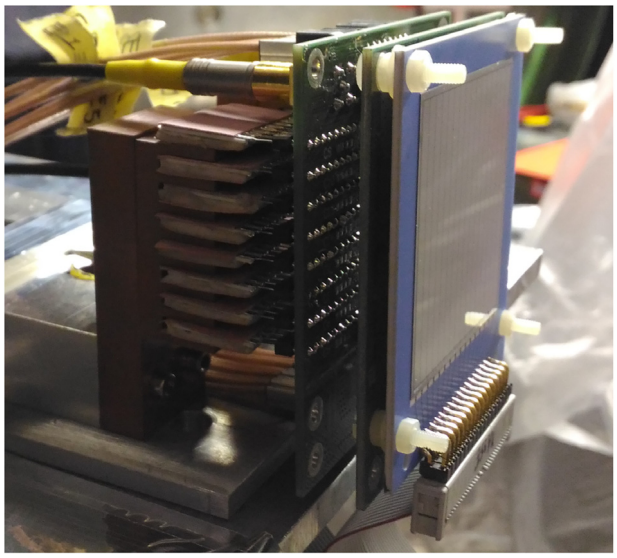

Fig. 4. A picture of the OSCAR device in the complete configuration. The strip detector and the first detector board are bounded with 4 screws, while the detector stages are connected to the rear board via two SMC Type Q connectors. The passive heat sink is visible in the photo.

these conditions we observed total leakage currents not exceeding 10 nA with all the strips simultaneously biased. The output signals of the pre-amplifier are then connected, by means of 2 groups of SCI coaxial cables, to 16 repetitions of a NIM front-end electronics with a spectroscopy amplifier.

The second detection stage consists of 16 independent silicon pad detectors manufactured by the Hamamatsu company with an active area of 1 cm^2 and a ceramic package. The width of the ceramic frame is 1.4 mm except for the bottom side, for which a 3.2 mm frame is required to host the connection pins. The silicon pads are welded, with a tolerance of about 0.1 mm, on a printed circuits board (first layer of Fig. 3), manufactured by the INFN-Sezione di Napoli, containing electronic lines for the Si-pad connections. To minimize the cross-talk level, each detector has an independent ground line parallel to the corresponding signal line. The SSSSD is anchored to the board containing the silicon pads as in Fig. 4, while the board is connected, by means of two SMC Type Q connectors, to a second board with embedded pre-amplifiers. This type of plug-and-play connection allows, with great versatility, to easily couple the detector stages with the pre-amplifiers board. Two sets of 8 Hamamatsu H4083 charge sensitive pre-amplifiers with 22 mV/MeV sensitivity and a low power consumption (150 mW maximum) are connected to the rear board by means of 9-pins single line type connectors. A ±6 V service voltage is given to the pre-amplifiers with two lemo connections on the rear side of the board, while a further lemo connection is also present to deliver a pulser signal to the electronic channels of the silicon pads. The signals from the second detection stage are collected via SCI connectors and delivered to a 16 channel Mesytec spectroscopic amplifier with integrated logic lines for generating the trigger signals and the corresponding gate for the acquisition system. Each pre-amplifier is dressed with a special material, thermally conductive and electrically insulating, in order to optimize the thermal contact with a copper heat sink, used as passive cooling system. It is clearly visible in the photo of Fig. 4, where the complete version of OSCAR is shown.

The geometry of OSCAR is determined by the possible crossings between strips and pads. In particular, all the possible overlap of a pad and the corresponding strip identify 64 ΔE–E pseudo-telescopes. A detailed geometrical scheme is described in Fig. 5, where the active area of each pad is represented by red squares, while blue lines delimit the active areas of each strip.

As visible from the figure, strips and pads are not exactly in geometrical matching. For example, the upper and lower parts of the second detection stage are not completely covered by the first stage. This explains the decreasing in the yield for the first and last rows of pseudo-telescopes observed in Fig. 6, which displays the number of identified particles for each pseudo-telescope obtained during a test experiment of OSCAR with heavy ion reactions (see the Section 2.2 for further details). A reduction of the active detection area is also expected for the first and last pseudo-telescopes of each quartet formed by a given pad and 4

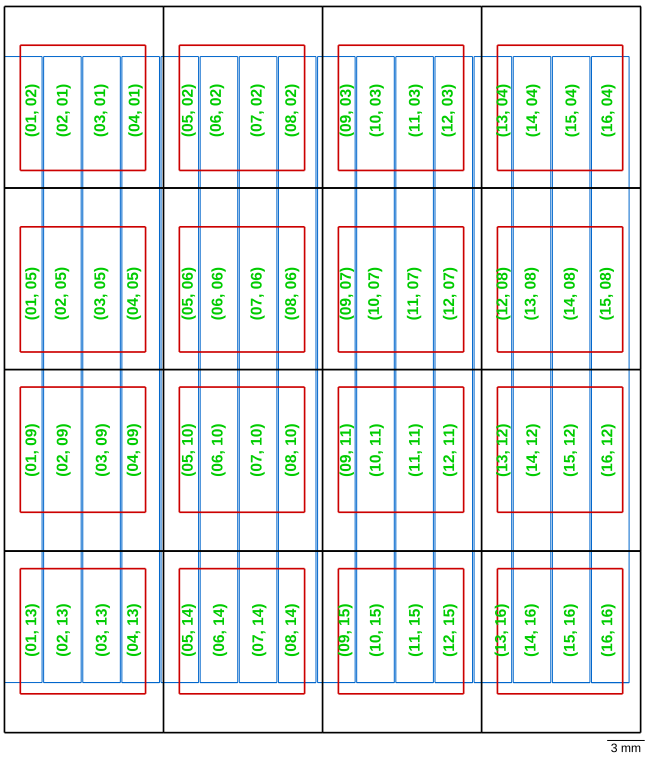

Fig. 5. A schematic view of the OSCAR telescope. The active area of each strip is delimited by a blue line, while each pad of the second detection stage is represented by a red square. Black lines represent the limits of the epoxy frame. Each pseudo-telescope is indicated by a label ($\#strip, \#pad$). (For interpretation of the references to color in this figure legend, the reader is referred to the web version of this article.)

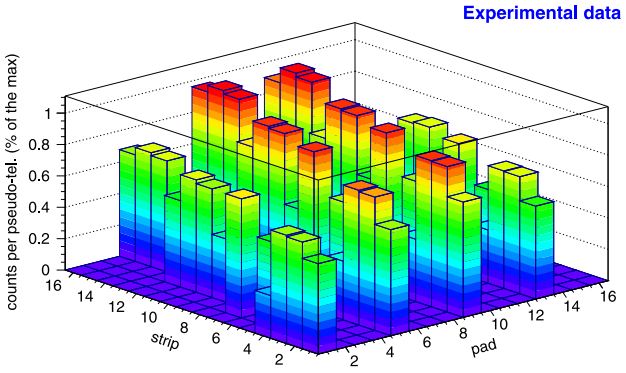

Fig. 6. Identified particle yield distribution on the ($\#strip, \#pad$) plane with experimental data taken in the test experiment described in Section 2.2.

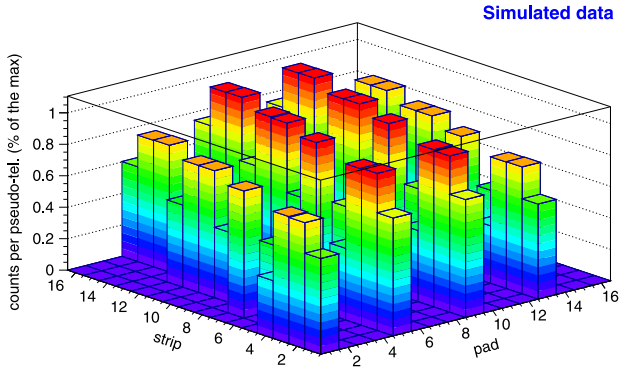

Fig. 7. Simulated detection efficiency represented on the ($\#strip, \#pad$) plane. The plot is obtained by filtering flight directions isotropically generated with a Monte Carlo code simulating the geometrical set-up and the characteristics of the OSCAR detector.

consecutive strips, because of the overlap with the ceramic frame of the pads, as seen in Fig. 5. This results in the yield trend shown in Fig. 6, where the population of the first and last pseudo-telescope of each quartet is significantly lower than central ones, reflecting the previously discussed geometrical details. In Fig. 7 we report a lego-plot analogous to Fig. 6 but obtained with a Monte Carlo procedure where a complete simulation of the OSCAR geometry is considered. Our simulation is based on the random isotropic extraction of emission directions in the space, filtered by using a pure geometrical software reproduction of OSCAR in which we carefully take into account the active areas of strip and pads and their superposition, with the prescriptions of Fig. 3. The two plots are in nice agreement, indicating that the relative efficiency in the particles identification, observed for the various pseudo-telescopes, can be attributed to pure geometrical effects. Furthermore, the average reduction of the yield for decreasing strip numbers, seen in the experimental spectrum of Fig. 6, can be attributed to the kinematics of nuclear collisions involved, being the polar detection angle increasingly larger while the strip number decreases (see the Section 2.2 for details about the present test experiment). This effect, that requires an accurate modeling of the reaction dynamics, is not included in the simulation.

2.2. Detector characterization

A first test, aimed to probe the energy resolution and general capabilities of the silicon pads, has been carried out for the second detection stage standalone by means of a three peaks α-source. α particles with energies of the order of 5.5 MeV are indeed stopped in 300 μm of silicon, and a measure of their total energy is possible. A pulse shape inspection with a digital oscilloscope of signals processed by the spectroscopy amplifiers allows to estimate the signal/noise ratio and also the level of the cross talk between connection lines. In particular, we obtained average noise levels of the order of 0.3% of signal amplitudes (and not exceeding 0.6% level) when the pads were irradiated by 5.48 MeV α particles at a rate of ≈ 300 Hz on the whole pad layer. These very low noise values indicate that the resolution of pads is not strongly affected by cross talks, thanks to the above discussed design of the boards.

A test of the cooling systems of pre-amplifiers has been also done by keeping the detector working under vacuum for few days. The measured temperatures at both the SSSSD and Si-pads pre-amplifiers reached a saturation value of, respectively, ≈ 30 °C and ≈ 40 °C after 24 hours.

The capabilities of OSCAR in terms of isotopic and energy resolution have been tested in several ways. In a first experiment OSCAR was used to detect fragments and light charged particles in Ca + Ca collisions at 35 MeV/nucleon. ^{40}Ca and ^{48}Ca beams were accelerated by the superconductive cyclotron K-800 of INFN-LNS, impinging on ^{40}Ca and ^{48}Ca targets. OSCAR was placed at $\theta = 55°$ in the laboratory frame at a distance of 103 cm from the target, while, simultaneously, the 4-blocks configuration of the FAZIA array was used at forward angles.

A typical ΔE–E plot obtained in this experiment is shown in Fig. 8 for a pseudo-telescope of OSCAR (E_{res} being the residual energy measured in the Si-pad). As clearly visible, lines corresponding to light nuclei are highly populated while, essentially due to kinematics, the statistics is lower for heavier ions. Particles with different Z values are unambiguously identified up to the punch-through points (except for the $Z = 1$ isotopes, for which the lines overlap the punch-through line of ^{4}He before their punch-through points), and a nice isotopic separation is also evident.

It is important to specify that with the term *identified particle* we indicate a couple of signals (ΔE and E_{res}) for which it is possible to reconstruct an unambiguous track inside OSCAR. The construction of tracks is based on a specific geometrical coherence algorithm, and we define *unambiguous* a track when it is the only one that is possible to construct with each used signals, as discussed in the Section 3.1.

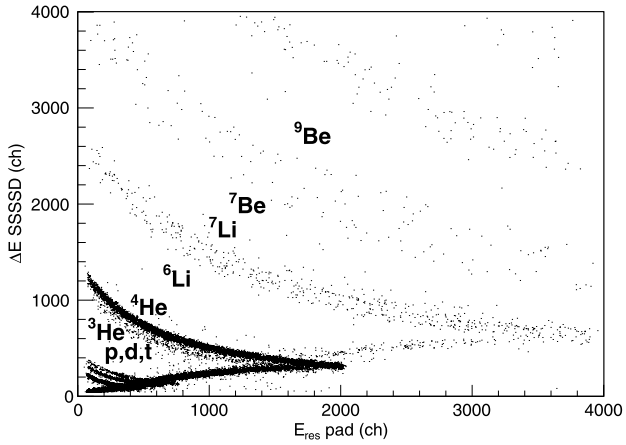

Fig. 8. ΔE–E plot for a pseudo-telescope of the OSCAR device. In the y-axis we report the signals released in the SSSSD stage, while in the x-axis we report the residual signals in the pads stage. Lines relative to identified isotopes are indicated by labels.

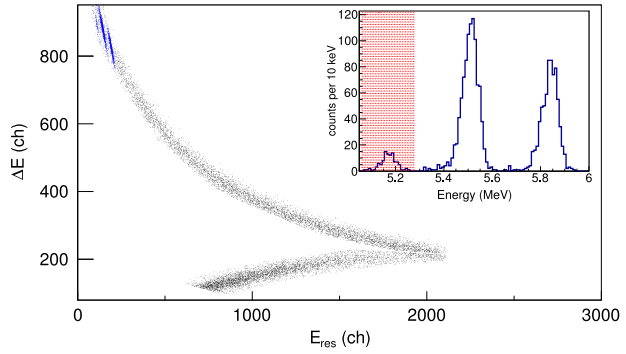

Fig. 9. ΔE–E_{res} plot for nuclei identified as ^{4}He. Blue points represent data taken during a calibration run in which the OSCAR device was irradiated by means of a 3-peaks α-source. The insert shows an energy spectrum obtained for ^{4}He detected in the calibration run. The area colored in red represents the energy region in which we observe a suppression of the yield due to the experimental identification limit at low energies. (For interpretation of the references to color in this figure legend, the reader is referred to the web version of this article.)

Energy calibrations for each strip and pad were obtained from punch-through points of various isotopes, assuming a total thickness given by the sum of the thickness of the Si-pad detectors and the measured thickness of the SSSSD (see Section 2.3) in correspondence of the pseudo-telescope analyzed. Calibrations have been complemented also by using a 3-peaks α-source, taking also into account the dead layer quoted in the previous paragraph. These particles are close to the punch-through in the SSSSD stage and therefore they release a large part of their energy in the first detection stage, while only weak signals are produced in the second stage; this allows to extend the calibration of the second stage at lower energies.

In Fig. 9 we report results concerning the detection of ^{4}He nuclei. Blue points come from a dedicated run in which OSCAR was irradiated by a 3-peak α-source containing a mix of ^{239}Pu, ^{241}Am and ^{244}Cm isotopes ($E_\alpha =$ 5.1 MeV, 5.5 MeV and 5.8 MeV). As visible, α particles occupy three different region of the ^{4}He line, reflecting the three different energies of the source. Furthermore, the lower energy peak is partly cut. This effect is due to the identification threshold. Indeed, α particles of $\approx$ 5 MeV are at the limit of identification of OSCAR, and, for this reason, only the most perpendicular flight directions can give signals in the second stage.

In the insert of Fig. 9 we show the spectrum obtained by summing the calibrated energy signals of the two stages for the α-source data. The red region indicates the part of the spectrum affected by the identification

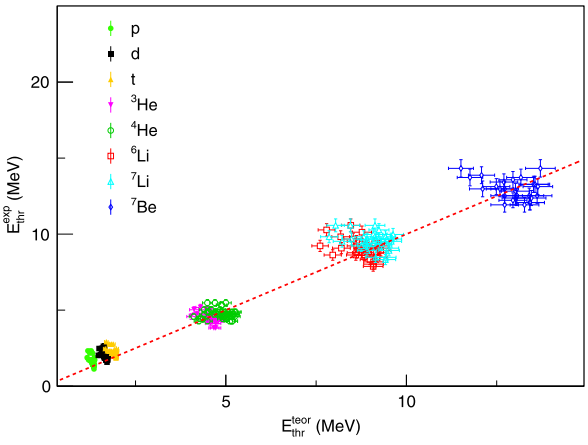

Fig. 10. Correlations between expected theoretical and experimental identification thresholds for different identified isotopes (see the legend) and for each pseudo-telescope. Error bars in the experimental values ($\approx$ 3%) accounts for indeterminacy on the energy calibration, while the calculated theoretical ones (3–5%) are affected by the indeterminacy of the detector thickness. The red dashed line represents the ideal trend for $E^{exp}_{thr} = E^{theor}_{thr}$.

threshold. For the 5.5 MeV peak we can estimate a global energy resolution of $\approx$ 70 keV FWHM, indicating the good performances of the detector.

In Fig. 10 we report the experimental identification thresholds of the OSCAR array for H, He, Li and Be isotopes; they correspond to the punching-through energies in the 20 μm first silicon stage for each identified nucleus and for each pseudo-telescope. We plot experimental values as a function of the ideal ones, taking only into account the thickness of the first detection stage (as experimentally measured, see next subsection). Error bars in the theoretical values of thresholds are calculated taking into account the detector non-uniformities, and they lies in the interval 3–5% depending on the type of particle and the gradient thickness in the SSSSD zone identifying a given pseudo-telescope. Experimental values (y-axis) are determined from the starting points of each reconstructed energy distribution; for these values we assumed a maximum (conservative) indetermination of 3% in agreement with the uncertainties in the energy calibrations and in the assignment of the spectra starting points. The behavior of the experimental points (in different colors for different isotopes) does not evidence any sizeable systematic divergence from the ideal trend $E^{exp}_{thr} = E^{theor}_{thr}$ shown by the bisector line (dashed red line), indicating negligible effects due to electronic non-linearities as well as to the entrance dead layer.

2.3. Non-uniformity of the ΔE stage

When ultra-thin Silicon detectors are used, it is mandatory to fully characterize their thickness uniformity [41–43]. To this aim we performed a dedicated experiment to obtain a precise characterization of the thickness of the first detection stage of the OSCAR detector. The SSSSD was mounted on a movable support which allowed to set, with a micro-metric accuracy, the spatial position of the SSSSD respect to a mono-isotopic α-source. A high resolution Si detector was placed in axial correspondence to the source, with the SSSSD placed between them. The α-source and the Si detector were both collimated with circular brass diaphragms of 1.0 mm radius. The thickness of the SSSSD was determined in different points of silicon surface, with 1 μm maximum uncertainty, by measuring the residual energy of α particles passing through the silicon layer and using energy loss routines.

Energy calibration of the Si detector was obtained by using α particles with different energies. A ^{239}Pu, ^{241}Am, ^{244}Cm α-mixed source was used to obtain high energy calibration points, while a ^{241}Am α-source followed by a calibrated 10 ± 0.5 μm Al foil was used to complement the calibration data set with a lower energy point.

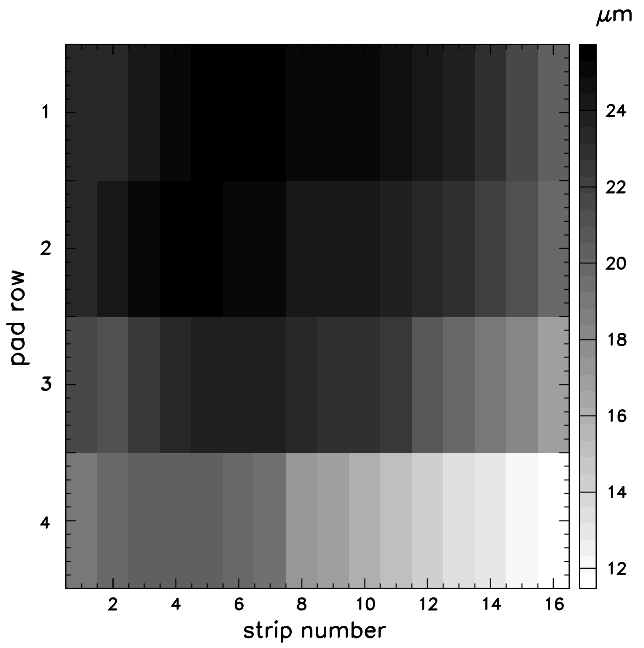

Fig. 11. Bi-dimensional distribution of the SSSSD thickness in the $(\#strip, \#pad)$ plane. The gray scale indicates the thickness, numbers are expressed in μm.

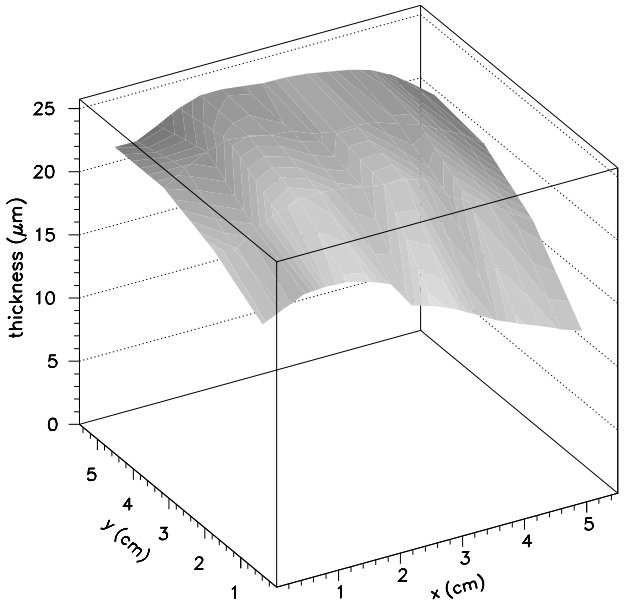

Fig. 12. SSSSD thickness characterization in the cartesian coordinates frame. The y-axis increases for increasing pad number while the x-axis is perpendicular to the strips direction. Thickness levels are expressed in μm and are represented on the z-axis. The picture puts in evidence the strong thickness gradient observed in correspondence of the right bottom corner of the detector.

With this apparatus, we were able to measure the SSSSD thickness in different points of its surface with 2 mm spatial indeterminacy. We performed 64 measurements at positions corresponding to the centers of each pseudo-telescope. The detector thickness for each point was calculated using the LISE++ software [44] from the measured residual energies. In doing this, we assumed that the whole SSSSD (including the thin Al layers used for electrical contacts) is made by silicon. Results are shown in Fig. 11, where the measured thickness is indicated in μm by the gray scale, and in the 3-dimensional representation of Fig. 12. Both figures indicate the presence of strong variation of the thickness, that

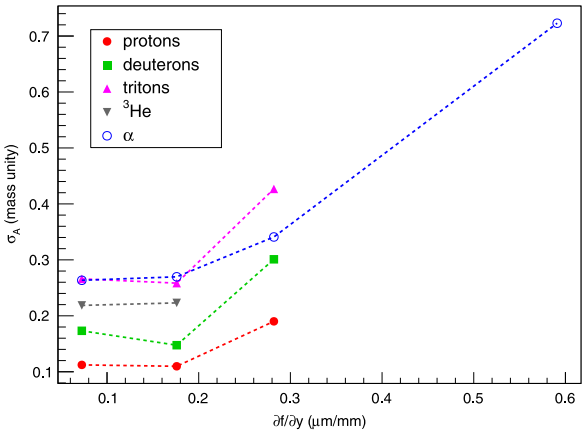

Fig. 13. Mass identification resolution σ_A (in unity of number of masses) as a function of the degree of non-uniformity of the first silicon stage, expressed as the thickness gradient along the strip direction $\partial f/\partial y$ in μm/ mm. Each $\partial f/\partial y$ value is given in correspondence of each pseudo-telescope center identified by the same strip. Different isotopes are reported in different colors as indicated in the legend. Error bars are not drawn.

reaches a minimum in the right-bottom corner of the SSSSD. This effect is attributed to the difficulties of manufacturing very thin (and large) slices of silicon. Thickness varies from 11.5 μm to 25.6 μm, pointing out a non-uniformity level well larger than the nominal one (±5 μm).

We estimate also how the isotopic resolution is affected by the SSSSD non-uniformities. In fact, the thickness uniformity of the ΔE layer directly affects the ΔE–E identification capability of a telescope. A way to quantify this effect is to correlate the isotopic resolution as a function of the thickness gradient.

An estimate of this gradient was obtained by carefully measuring the thickness of SSSSD at 10 positions along a given strip, thus obtaining an accurate thickness profile of a single strip. We selected the strip #14, that is sufficiently far from the border of the SSSSD, and has the maximum thickness excursion. The results were then interpolated with a polynomial function $f(x, y)$, being y the position along the pad row of Fig. 11, i.e. along the strip length, and y the one along the strip number axis. The thickness gradient along the direction of the strip can be deduced by partial derivative of this function: $\partial f/\partial y$. For each pseudo-pixel we have considered the value that the derivative assumes in the corresponding center.

To quantify the isotopic resolution, we transformed the points of the ΔE–E scatter plot into mass spectra. To this aim we used an analytical method [45]. Firstly, we find a set of parameters of a Bethe–Bloch based function that reproduce the shape of each line in the ΔE–E plot; secondly, we consider the distance of each experimental point in the ΔE–E plane with the corresponding analytical line. For a given isotope, an estimate of the mass resolution is thus obtained as the σ_A of its mass distribution extracted from a Gaussian fit. We report in Fig. 13 σ_A (in unity of number of masses) as a function of the thickness gradient $\partial f/\partial x$ (in μm/ mm). As expected, the trend indicates an increase of the σ_A values for each isotope as the non-uniformity level increases. More precisely, we observe that a uniformity better than 0.3 μm/ mm is mandatory to obtain a good identification of isotopes up to ^{4}He when we use a module of OSCAR. Above this value the $Z = 1$ lines merge together, while we can still estimate $\sigma_{^4He}$ because of the very low ^{3}He emission respect to ^{4}He. Unfortunately, this type of analysis cannot be performed on Li and Be isotopes because of the low collected statistics.

2.4. Channeling effects in ΔE detector

While ions move inside a silicon crystal, atomic planes could line up offering to the ions preferential ways to pass through the crystal with a reduced interaction with atomic electrons and nuclei. This effect is

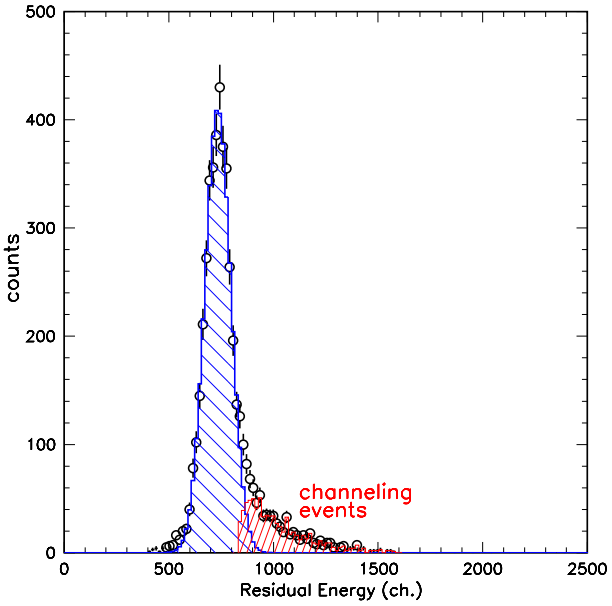

Fig. 14. Channeling effect studied from the residual energy spectrum, for one of the measured points. The blue line represents the normal (unchanneled) contribution to the spectrum, parametrized with a Gaussian curve (open circles). Channeling events are associated to the non-Gaussian tail of the spectrum (red area). (For interpretation of the references to color in this figure legend, the reader is referred to the web version of this article.)

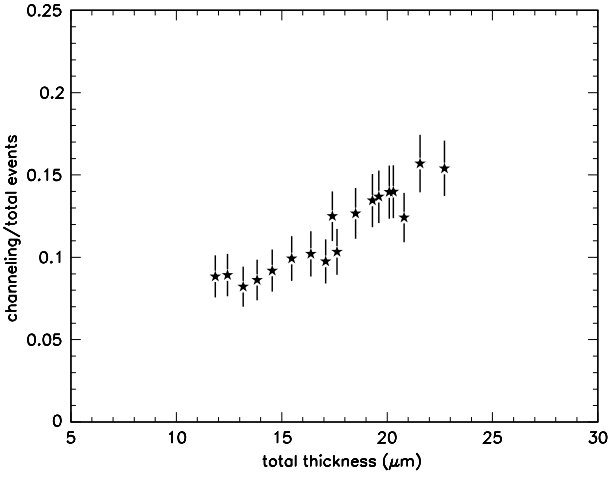

Fig. 15. Evolution of the percentage of channeling events as a function of the detector thickness.

known as *channeling*, and results in a reduction of the expected energy loss [46]. As shown in Ref. [47], the evaluation of such effects is very important for particle identification and for the design of new silicon detectors. In fact, in the ΔE–E technique, channeling effects introduces fluctuations that worsen the isotopic resolution.

The presence of channeling effects can be seen by inspecting the shape of α particle energy spectra after passing through the ΔE stage. To do this we used the same geometrical set-up described in the previous paragraph and a ^{241}Am α source. A typical energy spectrum is displayed on Fig. 14; it corresponds to a region of the ΔE detector having 21 μm thickness. In absence of channeling, this spectrum should have a Gaussian shape due to the statistical nature of the energy loss mechanisms for thick layers; at variance, in presence of channeling, a high energy tail appears. Indeed, this last case is experimentally observed. To estimate the relative yield of the channeling events, we performed a Gaussian fit (blue solid line) of the experimental points (open circles); the upper limit of the fit region was set around the right

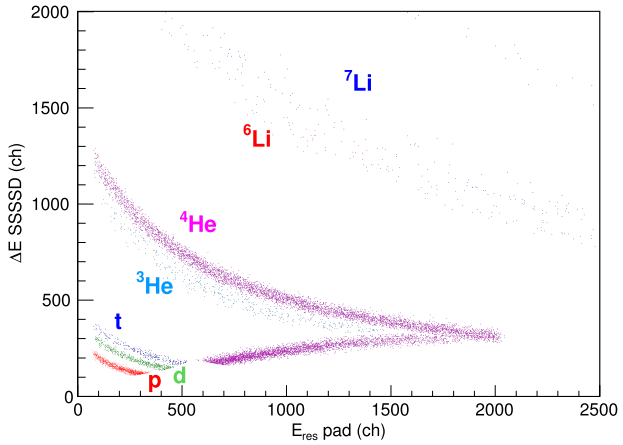

Fig. 16. ΔE–E spectrum for a pseudo-telescope of OSCAR, with the particles used in the for the data analysis. These particles fulfill the track selection criterion explained in the text. The ^{4}He passing through the first two detection stages are identified up to just before the overlap with the punch-through points of hydrogen isotopes. Lines are presented with different colors and indicate the corresponding identified isotope. (For interpretation of the references to color in this figure legend, the reader is referred to the web version of this article.)

half-maximum point of the spectrum. The channeling yield was then estimated by subtracting the Gaussian component from the experimental data. This contribution is reported on Fig. 14 with the red spectrum.

The percentage of channeling events is, in this case, 15 ± 3%; this value is in reasonable agreement with the ones estimated in [48] for similar silicon thickness and a similar geometrical setup. An overall view of the percentage of channeling events as a function of the silicon thickness is reported in Fig. 15. Even if the error bars are quite large, we see a correlation between the thickness of the silicon detector and the percentage of channeling events, at least in the thickness domain here explored (12–22 μm). This finding is in agreement with the one of Ref. [48] and seems to indicate that the channeling plays a minor role in the case of ultra-thin detectors (< 15 μm).

3. Results from Ca + Ca data analysis

In this section we discuss results obtained by analyzing data from Ca + Ca collisions at 35 MeV/nucleon. As previously anticipated, this analysis will involve mainly the study of particles and fragments emitted from the quasi-target (QT) source; it is possible to do profitably this work thanks to the low identification threshold of the OSCAR hodoscope.

3.1. Energy spectra of the lightest isotopes

To correctly reconstruct the energy and emission angle of each emitted particle, we have developed a specific algorithm for the definition of a track inside the OSCAR device. Indeed, being OSCAR constituted by a stage of Si strips followed by a second stage of Si pads, one has to select the right couples of signals given by the detectors that individuate physical particles. To explain the geometrical procedure developed to reconstruct unambiguous couples of signals we recall the scheme of Fig. 5. It is possible to clearly identify 4 quartets of strips which cover each of the 4 vertical quartets of pads. In other words, each pad insists on 4 different strips. For this reason, the only way to identify unambiguously a particle inside OSCAR is that only a single strip and a single pad give a signal in the same quartet. In this way it is possible to define a track, discarding events in which an ambiguity is present. We verified that, thanks to the low event rate, the number of rejected events is very small and does not affect noticeably the statistics. The following analysis is carried out by using well characterized events with well identified particles.

Fig. 16 shows the regions populated by these particles in the ΔE–E plane by selecting a pseudo-telescope. We see that the lines of lithium

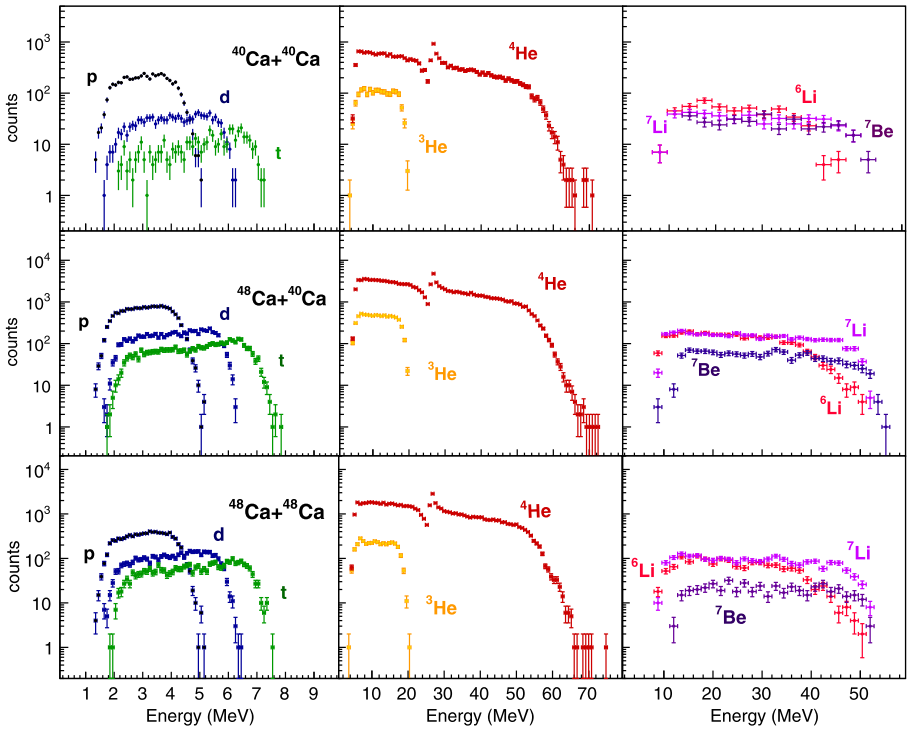

Fig. 17. Energy spectra of identified particles up to ^{7}Be. In the top, mid and bottom rows we report, respectively, spectra for ^{40}Ca + ^{40}Ca, ^{48}Ca + ^{40}Ca and ^{48}Ca + ^{48}Ca nuclear systems. Experimental data are plotted in different colors and the corresponding isotopes are indicated by labels. ^{4}He energy spectra have been extended above the punch-through point. (For interpretation of the references to color in this figure legend, the reader is referred to the web version of this article.)

isotopes have still a reasonable isotopic separation Concerning beryllium isotopes, due to the absence of ^{8}Be, it is still possible to identify ^{7}Be events (here not shown for clarity reasons). Energy spectra of light isotopes are shown in Fig. 17. Spectra of isotopes of $Z = 1, 2, 3$ are shown from the left to the right, are ordered from top to bottom, while data from ^{40}Ca + ^{40}Ca, ^{48}Ca + ^{40}Ca and ^{48}Ca + ^{48}Ca nuclear systems are plotted, respectively, in top, medium and bottom panels. For the sake of simplicity, ^{7}Be energy spectra are reported together with the $Z = 3$ isotopes. Each spectrum shows a steep decrease of the yield at high energies, due to the punch-through of the second silicon stage by swift particles. The starting points of each energy spectrum is about 1.2 MeV/nucleon, a consequence of the very low identification thresholds discussed in Section 2.2. A special analysis was done to reconstruct the ^{4}He spectra. They have been obtained by summing events preceding and following the punch-through point. The incident energies of α particles passing through the second stage are calculated from the energy loss in both stages by using energy loss tables. This results in the presence of the *wing* at about 26 MeV, a region where particles having energies lower and higher than the punch-through one are in close vicinity and cannot be easily distinguished.

In the bombarding energy domain here explored, and in presence of semi-peripheral collisions (that geometrically dominates the events of reactions), we expect the emission of particles essentially from three sources moving at different velocities in the laboratory reference frame [5,12]. Quasi-target (QT) and quasi-projectile (QP) sources describe the emission of particles by residues of projectile and target nuclei after the collision has occurred. The emission of particles by these sources suggests that they move with velocities approaching the initial target (in the case of QT) and projectile (in the case of QP) nuclei. A third source of emission, named mid-velocity (MV) source is commonly observed and has been the subject of intense investigations both theoretically and experimentally [49–51]. Such source seems to move at center of mass velocity between the QT and QP sources. QT emissions are commonly observed as being characterized by an evaporative process and the corresponding products are almost isotropic and with low energies also in the laboratory frame. A clue of the good capabilities of OSCAR in the detection of such particles can be obtained by analyzing the kinetic energy spectra in terms of moving sources with Maxwellian shape, as discussed in [5,52]. Clearly, limited by our geometrical acceptance, we cannot make selections on the impact parameter of the collisions and, for this reason, we have performed our analysis only to inclusive events. Anyway, semi-peripheral events provide a dominant contribution to the total reaction cross section. As a first approximation, which is well reasonable for our purposes, we analyzed ^{4}He energy spectra. We focus on the data of the ^{48}Ca + ^{48}Ca system, having the highest statistics. The fit has been performed by including three Maxwellian moving sources, Eq. (1), corresponding to the evaporative emissions by the three sources QT, MV and QP mentioned above [52,53]:

$$Y(E_{lab},\theta) = \sum_{i=1}^{3} N_i \sqrt{E_{lab} - E_C} \quad \times \\ exp\left[-\frac{E_{lab} - E_C + E_{S,i} - 2\sqrt{(E_{lab} - E_C)E_{S,i}} \times cos\theta}{T_i}\right] \quad (1)$$

Each of the three terms, $i = 1, 2, 3$, represents the contribution to the observed yield of a specific isotope having mass m and charge Z, emitted at an angle θ in the laboratory frame within a solid angle $d\Omega$ and with kinetic energy $E \in [E_{lab}, E_{lab} + dE_{lab}]$. T_i indicates the temperature of the ith source while $E_{S,i} = (1/2)mv_S^2$ is the non-relativistic kinetic energy of a particle having mass m and velocity equal to the one ($v_{S,i}$) of the ith source in the laboratory frame. $E_C = ZE_{coul}$ is a term representing the energy needed by the particle to overcome the Coulomb barrier. N_i, normalization coefficients which regulate the weight of each contribution to the emission spectrum, are used as free parameters in our fit procedure, with the constraint $N_{QP} = N_{QT}$, imposed by the symmetry of the studied reaction system. The parameters $E_{coul} = 4$ MeV, $T_{QP} = T_{QT} = 5.5$ MeV and $T_{MV} = 10.5$ MeV, taken from systematics reported in the literature [53–56], were constrained in our fit procedure. The velocities $v_{S,i}$, also used as fixed values, are calculated with the prescription discussed in [53] as follows: for v_{QP} we used the 75% of the beam velocity $\beta_{QP} \approx 0.19$ and, as a consequence from the symmetry

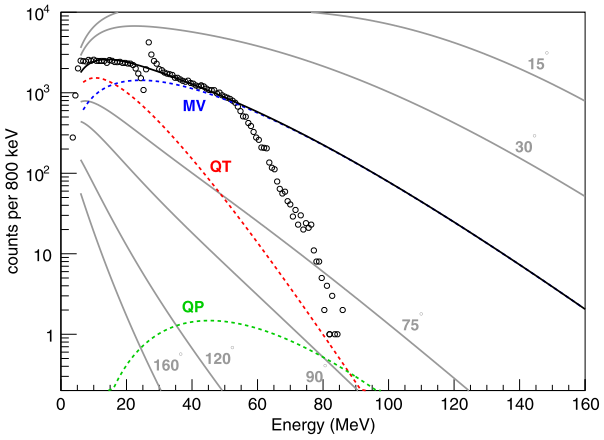

Fig. 18. Inclusive ^{4}He energy spectrum obtained from the ^{48}Ca + ^{48}Ca system at 35 MeV/u, and measured at $\theta = 55°$ (black open circles). The spectrum is reproduced by a three Maxwellian moving sources fit (black line). QT, MV and QP components are shown respectively with the red, blue and green dashed lines. Gray lines are used to show the expected total yields at different angles. (For interpretation of the references to color in this figure legend, the reader is referred to the web version of this article.)

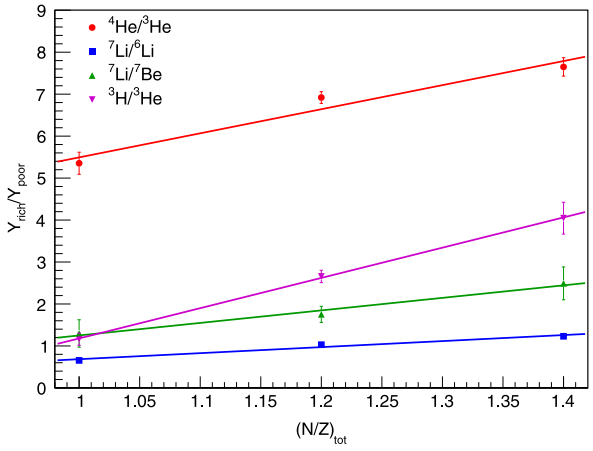

Fig. 19. Isotopic (^{4}He/^{3}He and ^{7}Li/^{6}Li) and isobaric (^{7}Li/^{7}Be and ^{3}H/^{3}He) yield ratios as a function of the $(N/Z)_{tot}$ for ^{40}Ca + ^{40}Ca, ^{48}Ca + ^{40}Ca and ^{48}Ca + ^{48}Ca systems at 35 MeV/nucleon. Lines represents a *best-fit* of the data and guide the eye. (For interpretation of the references to color in this figure legend, the reader is referred to the web version of this article.)

of the reaction, $\beta_{QT} \approx 0.07$ and $\beta_{MV} = (1/2)\beta_{beam} = 0.13$. Finally we considered a fixed value of $\theta = 55°$ for the whole hodoscope, being $\Delta\theta \approx 1°$ the corresponding angular acceptance of OSCAR in the used geometrical configuration. This first approximation procedure allows to produce the fit reported in Fig. 18, where the experimental spectrum of ^{4}He (black open circles) is shown together with the result of the fit (black solid line). Dashed lines are plotted to show the contributions due to QP (blue line), MV (green line) and QT (red line) sources. Gray lines show the corresponding expected ^{4}He energy spectra, computed with the same parameters of the present fit, for different angles in the laboratory frame. We observe a good agreement in the energy region from 4 MeV to 60 MeV, where the measured yield is almost insensitive to efficiency effects. We also observe that in the range 4 MeV $\leq E \leq$ 20 MeV the spectrum is dominated by emissions from the QT component while, above 20 MeV, emissions from the MV source become dominant. We verified that the shape of the low energy part of the experimental spectrum cannot be reproduced only by assuming the presence of a QP and MV source, or the presence of a QP and a fusion-like source. This finding, even if in a qualitative fashion, underline the capability of OSCAR to detect very low energy particles emitted by the QT source in heavy ion collisions.

3.2. QT isobaric and isotopic ratios: Isospin diffusion effects

An indirect and efficient way to probe the neutron enrichment of an excited nuclear source consists of studying the N/Z ratio of its emitted fragments. In particular, isobaric and isotopic neutron-rich/neutron-poor yield ratios can be used as sensitive probes of the N/Z ratio of the corresponding emitting source [5,14].

As previously discussed, our detector is sensitive to the particle emissions from the QT source. Because of the limited angular coverage of OSCAR, we deduced the QT emission yield for several isotopes by integrating the spectra in kinetic energy windows where the QT emission is expected to dominate. For each isotope, we estimated these integration limits with the Maxwellian fit procedure outlined previously. Furthermore, we have restricted the integration regions to energy intervals of equal width for each investigated couple of isotopes/isobars; we discarded region affected by efficiency effects.

Fig. 19 shows isotopic and isobaric yield ratios (plotted in different colors) as a function of the $(N/Z)_{tot}$ of the total system formed in the collision ($(N/Z)_{tot} = 1$ for ^{40}Ca + ^{40}Ca, $(N/Z)_{tot} = 1.2$ for ^{48}Ca + ^{40}Ca and $(N/Z)_{tot} = 1.4$ for ^{48}Ca + ^{48}Ca). Lines serve to guide the eye.

Under the hypothesis that the observed ratios reflect the isospin content of the QT source, we can deduce the presence of isospin transport effects. Each ratio, in the case of the mixed system ^{48}Ca + ^{40}Ca, results in intermediate values between the two symmetric systems. This finding indicates that the neutron excess of the projectile (^{48}Ca) influences the neutron content of the QT (the target being ^{40}Ca) source during the interaction phase. This effect can be explained, as shown in [5,53,55] by assuming that a net neutron flux goes from the neutron-rich to the neutron-poor collision partner (*isospin diffusion*). These results demonstrate the capability of performing isospin transport studies with the OSCAR hodoscope. In particular, the coupling of several OSCAR modules at very backward angles with high coverage arrays (as FAZIA) at forward angles could represent a powerful set-up to investigate isospin diffusion phenomena by simultaneously reconstruct the emission of particles and fragments from the QP and the QT sources for dissipative binary collisions.

3.3. Correlations: The case of α-α correlation and the reconstruction of ^{8}Be

Particle–particle and multi-particle correlations are topics of great interest in heavy ion collisions from both the experimental [29,57,58] and the theoretical point of view [59,60]. They allow not only to investigate on the structure of resonant states produced in nuclear collisions but also on the space–time properties of the nuclear medium itself. In this Paragraph we report on the possibility of taking advantage from the good energy resolution and angular segmentation of the OSCAR hodoscope to investigate the decay of resonances produced in the collisions by means of the invariant mass technique [25]. In particular, we discuss the reconstruction of ^{8}Be via the α-α correlation. In Fig. 20 we show the α-α invariant mass spectrum obtained by selecting couples of α particles; to increase the statistics we summed events from all the colliding systems. For simplicity, we show it in terms of *relative energy*, i.e. the kinetic energy of the particles in the reference of the emitting source, which is defined as $E_{rel} = w - \sum m_i$, being w the invariant mass of the system and m_i mass of the ith particle. As expected, we found a peak centered at about 90 keV, which corresponds to the ground state of ^{8}Be produced in the collisions. Unfortunately, due to the limited angular coverage of the hodoscope, placed at a distance of 103 cm from the target, we collected a low statistics and we are not sensitive to the first excited state of ^{8}Be, located at around 3 MeV. If a couple of α particles is emitted from this latter state we are indeed not able to simultaneously detect the two particles, being the corresponding kinematical cone larger than the angular acceptance of our detector.

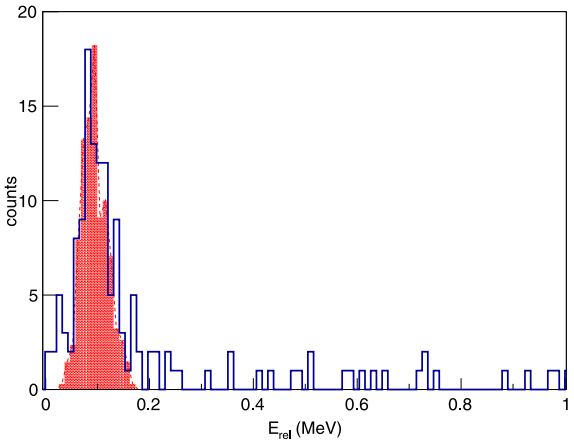

Fig. 20. α-α invariant mass spectrum (in the form of E_{rel}) obtained by summing the statistics from the three nuclear systems here studied. Data exhibit a peak at about 90 keV which corresponds to the ground state of ^{8}Be. The low statistics is due to the large distance of OSCAR from the target.

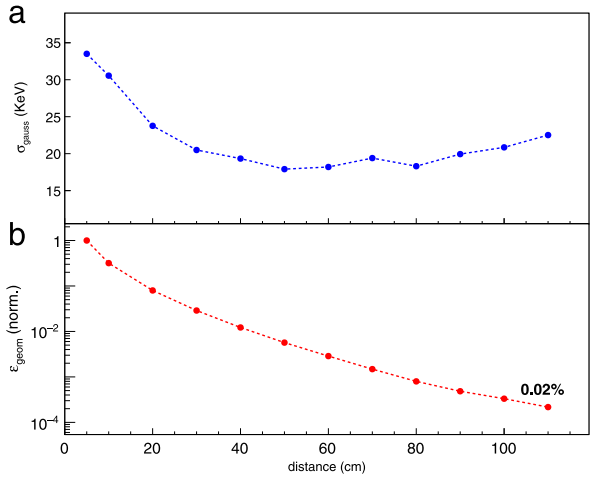

Fig. 21. (a) Resolution in the reconstruction of the ^{8}Be ground state via α-α correlations, extracted as the σ of a Gaussian fit, as a function of the distance of OSCAR from the target. (b) Same plot for the efficiency, normalized to the point at 5 cm. A value of 0.02% is reached at 110 cm.

The distance from the target to the OSCAR hodoscope is therefore a parameter of fundamental importance to be taken into account, for correlation studies, since it regulates not only the efficiency in the reconstruction of resonances but also the relative energy resolution. Being OSCAR a modular device, designed to be installed with high versatility in different configurations, a precise study of the above mentioned aspects as a function of the distance from the target is required to fully characterize the powerfulness of the device.

To this aim we developed a Monte Carlo code by using the previously discussed geometrical simulation of OSCAR as a filter to process simulated ^{8}Be decays data. To produce the set of simulated events, we have considered a flat angular distribution of the emitting ^{8}Be nuclei, having values of momentum extracted uniformly from 500 MeV/c to 1200 MeV/c, as suggested by the reconstructed ^{8}Be momentum spectrum derived from the experimental data of Fig. 20. The physical interaction of particles with the detector is not accounted in our procedure. The results of our simulation are reported in Fig. 21. The upper panel shows the relative energy resolution in the reconstruction of the ground state of ^{8}Be as a function of the distance from the target. With resolution we indicate the σ_{gauss} of a Gaussian fit reproducing the ground state peak seen in the invariant mass spectrum. Varying the distance from 5 cm to 110 cm we observe a decrease of the resolution from about 31 keV to about 9 keV, which represent a very good value. The simulation shows also that the expected resolution saturates for values of distance higher than 80 cm. This effect can be attributed to the reduced number of pseudo-telescopes which contribute to the spectrum; in fact, when the distance is larger the kinematical cone of the emitted particles becomes wider compared to the size of the detector. In the bottom panel we show the efficiency in the reconstruction of such resonance as a function of distance. In this case we have normalized the values to 100% at 5 cm from the target. The plot reveals a strong decrease of the geometrical efficiency with the distance. In correspondence of 110 cm it reaches the 0.02% of the value observed at 5 cm. Such plots are useful to fix the optimal distance for studying the decay of a particular resonance, and the versatility of OSCAR allows to reach a good balance between efficiency and resolution.

4. Conclusions and perspectives

In this paper we discuss the characteristics of the new hodoscope OSCAR aimed at the identification of low energy light particles emitted in heavy ion collisions. This new modular and high versatility device, based on two detection stages of silicon detectors (20 μm SSSSD followed by 300 μm silicon pads), has been designed to complement other larger acceptance detectors in the angular regions in which high segmentation and low identification thresholds are required. We provide a precise characterization of the thickness uniformity of the ΔE stage, showing how it affects the particles identification obtained with the telescope technique. From our analysis it turns out that, with such a segmentation, a thickness gradient up to 0.3 μm/mm can be tolerated to obtain reasonable identifications of p, d, t, ^{3}He and ^{4}He particles. Channeling effects have been also observed in the thin silicon strip detector used as first detection stage; the percentage of channeled to normal events is about 15% and slightly decreases with decreasing thickness of the detector.

Results from Ca + Ca collisions at 35 AMeV, obtained with OSCAR, are also discussed. They demonstrate the capability of OSCAR to identify low energy particles emitted by the *quasi-target* source in *semi-peripheral* collisions. We obtain signatures of the isospin diffusion process by inspecting isotopic (^{4}He/^{3}He and ^{7}Li/^{6}Li) and isobaric (^{7}Li/^{7}Be and ^{3}H/ ^{3}He) yield ratios of particles emitted by the QT source. We finally discussed the good performance of OSCAR in the reconstruction of resonances produced in nuclear reactions, via particle–particle correlations and invariant mass spectroscopy.

Recently, we used a modified version of OSCAR, based on 4 modules of OSCAR without the first detection stage, assembled in a 2 × 2 configuration, for studying the decay path of the Hoyle state in ^{12}C [61,62]. Invariant mass techniques have been used to unveil on the competition between direct and sequential decay modes, taking advantage from the good granularity of OSCAR and the extremely high versatility.

Acknowledgments

We kindly thank the Servizio Elettronica e Rivelatori of INFN-Naples division for their support in the development of the OSCAR device and the design of the boards. We thank the *late* Prof. E. Rosato (Federico II University of Naples) for his strong support during the commissioning phase of the prototype. We are strongly indebted to C. Marchetta, E. Costa and A. Massara, of the Target Service of INFN-LNS (Catania), for their invaluable support in the characterization of the strip detector.

References

[1] H.S. Xu, et al., Isospin fractionation in nuclear multifragmentation, Phys. Rev. Lett. 85 (2000) 716–719. http://dx.doi.org/10.1103/PhysRevLett.85.716. arXiv:nucl-ex/9910019.

[2] M.B. Tsang, W.A. Friedman, C.K. Gelbke, W.G. Lynch, G. Verde, H. Xu, Isotopic scaling in nuclear reactions, Phys. Rev. Lett. 86 (2001) 5023–5026. http://dx.doi.org/10.1103/PhysRevLett.86.5023. arXiv:nucl-ex/0103010.

[3] M.B. Tsang, et al., Isospin diffusion and the nuclear symmetry energy in heavy ion reactions, Phys. Rev. Lett. 92 (2004) 062701. http://dx.doi.org/10.1103/PhysRevLett.92.062701.

[4] M.B. Tsang, Y. Zhang, P. Danielewicz, M. Famiano, Z. Li, W.G. Lynch, A. W.Steiner, Constraints on the density dependence of the symmetry energy, Phys. Rev. Lett. 102 (2009) 122701. http://dx.doi.org/10.1103/PhysRevLett.102122701. arXiv:0811.3107; Internat. J. Modern Phys. E19 (2010)1631. http://dx.doi.org/10.1142/S0218301310016041.

[5] I. Lombardo, et al., Phys. Rev. C 82 (2010) 014608.

[6] D.V. Shetty, S.J. Yennello, G.A. Souliotis, Density dependence of thesymmetry energy and the nuclear equation of state: A dynamical andstatistical model perspective, Phys. Rev. C (2007) 024606. http://dx.doi.org/10.1103/PhysRevC76024606. arXiv:07040471; Phys. Rev. C76 (2007)039902; http://dx.doi.org/10.1103/PhysRevC76039902 Erratum.

[7] B.-A. Li, À. Ramos, G. Verde, I. Vidaña, Topical issue on nuclearsymmetry energy, Eur. Phys. J. A 50 (2) (2014) 9. http://dx.doi.org/10.1140/epja/i2014-14009-x.

[8] M. Baldo, G.F. Burgio, The nuclear symmetry energy, Prog. Part. Nucl. Phys. 91 (2016) 203–258. http://dx.doi.org/10.1016/j.ppnp.2016.06.006. arXiv:1606.08838.

[9] G. Prete, et al., Phys. Proc. 26 (2012) 274.

[10] Système de Production d'Ions RadioactifsAccélérés en Ligne,http://pro.ganil-spiral2eu/spiral2.

[11] The ISOLDE radioactive ion beam facility,http://isolde.web.cern.ch/.

[12] E. Galichet, et al., Phys. Rev. C 79 (2009) 064614.

[13] M. Veselsky, et al., Phys. Rev. C 62 (2000) 041605 (R).

[14] S. Barlini, et al., Phys. Rev. C 87 (2013) 054607.

[15] M. Tsang, et al., Phys. Rev. Lett. 102 (2009) 122701.

[16] J. Pouthas, et al., Nucl. Instrum. Methods A 357 (1995) 418.

[17] O. Lopez, et al., Phys. Rev. C 90 (2014) 064602.

[18] F. Grenier, et al., Nuclear Phys. A 811 (2008) 233.

[19] D. Gruyer, et al., Phys. Rev. C 92 (2015) 064606.

[20] G. Pasquali, et al., Nucl. Instrum. Methods A 570 (2007) 126.

[21] F. Salomon, et al., J. Instr. 11 (2016) C01064.

[22] G. Pastore, et al., Isotopic identification using Pulse Shape Analysis ofcurrent signals from silicon detectors: Recent results from the FAZIA collaboration, Nucl. Instrum. Methods A 860 (2017) 42–50. http://dx.doi.org/10.1016/j.nima.2017.01.048.

[23] E. De Filippo, A. Pagano, Eur. Phys. J. A 50 (2014) 32.

[24] G. Cardella, et al., Nucl. Instrum. Methods A 799 (2015) 64.

[25] D. Dell'Aquila, et al., Phys. Rev. C 93 (2016) 024611.

[26] D. Dell'Aquila, et al., EPJ Web Conf. 117 (2016) 06011.

[27] E.V. Pagano, et al., EPJ Web of Conf. 117 (2016) 10008.

[28] D. Dell'Aquila, Il Nuov. Cim. C 39 (2016) 272.

[29] L. Morelli, et al., J. Phys. G: Nucl. Part. Phys. 43 (2016) 045110.

[30] L. Morelli, et al., J. Phys. G 41 (2014) 075108.

[31] M. D'Agostino, et al., Nuclear Phys. A 861 (2011) 47–66.

[32] R.T. De Souza, et al., The MSU miniball 4 pi fragment detection array, Nucl. Instrum. Methods A 295 (1990) 109–122. http://dx.doi.org/10.1016/0168-9002(90)90429-A.

[33] B. Davin, R. de Souza, R. Yanez, Y. Larochelle, R. Alfaro, H. Xu, A. Alexander, K. Bastin, L. Beaulieu, J. Dorsett, G. Fleener, L. Gelovani, T. Lefort, J. Poehlman, R. Charity, L. Sobotka, J. Elson, A. Wagner, T. Liu, X. Liu, W. Lynch, L. Morris, R. Shomin, W. Tan, M. Tsang, G. Verde, J. Yurkon, Lassa:a large area silicon strip array for isotopic identification of chargedparticles, Nuclear Instruments and Methods in Physics Research Section a:Accelerators, Spectrometers, Detectors and Associated Equipment 473 (3) (2001) 302–318. http://www.sciencedirect.com/science/article/pii/S0168900201002959.

[34] D.D.S. Coupland, et al., Probing effective nucleon masses with heavy-ioncollisions, Phys. Rev. C 94 (1) (2016) 011601. http://dx.doi.org/10.1103/PhysRevC.94.011601. arXiv:1406.4546.

[35] M. Wallace, M. Famiano, M.-J. van Goethem, A. Rogers, W. Lynch, J. Clifford, F. Delaunay, J. Lee, S. Labostov, M. Mocko, L. Morris, A. Moroni, B. Nett, D. Oostdyk, R. Krishnasamy, M. Tsang, R. de Souza, S. Hudan, L. Sobotka, R. Charity, J. Elson, G. Engel, The high resolution array (hira) for rare isotope beam experiments, Nucl. Instrum. Methods Phys. Res. A 583 (2) (2007) 302–312. http://dx.doi.org/10.1016/j.nima.2007.08.248. http://www.sciencedirect.com/science/article/pii/S016890020701947X.

[36] S. Wuenschel, et al., Nucl. Instrum. Methods A 604 (2009) 578.

[37] A.B. McIntosh, et al., Phys. Rev. C 87 (2013) 034617.

[38] A.Z. Kohley, et al., Phys. Rev. C 82 (2010) 064601.

[39] L. Qin, et al., Phys. Rev. Lett. 108 (2012) 172701.

[40] A. Jedele, et al., Phys. Rev. Lett. 118 (2017) 062501.

[41] A. Matta, Ph.D. Thesis, Univ. Paris-Sud, 2012.

[42] A. Matta, et al., Phys. Rev. C 92 (2015) 041302 (R).

[43] A. Kordyasz, et al., Eur. Phys. J. A 51 (2015) 15.

[44] LISE + +, http://lise.nscl.msu.edu/lise.html.

[45] N. Le Neindre, et al., Nucl. Instrum. Methods A 490 (2002) 251.

[46] S. S. (Ed.), VLSI Technology, second ed., Mcgraw-Hill, New York, 1988.

[47] L. Bardelli, et al., Nucl. Instrum. Methods A 605 (2009) 353–358.

[48] G. Thungström, et al., Nucl. Instrum. Methods A 546 (2005) 312–318.

[49] S. Piantelli, L. Bidini, G. Poggi, M. Bini, G. Casini, P.R. Maurenzig, A. Olmi, G. Pasquali, A.A. Stefanini, N. Taccetti, Intermediate mass fragment emission pattern in peripheral heavy-ion collisions at fermi energies, Phys. Rev. Lett. 88 (2002) 052701. http://dx.doi.org/10.1103/PhysRevLett.88.052701. arXiv:nucl-ex/0105004.

[50] D.V. Shetty, et al., Mid-rapidity emission in 124 Sn, 124 Xe + 124 Sn, 112 Sn reactions at 28 MeV/nucleon, Nucl. Phys. A 734 (2004) E100–E103. http://dx.doi.org/10.1016/j.nuclphysa.2004.03.030.

[51] E. De Filippo, et al., Acta Phys. Pol. B 40 (2009) 1199–1207.

[52] G. Lanzanò, et al., Phys. Rev. C 58 (1998) 281.

[53] D. Shetty, et al., Phys. Rev. C 68 (2003) 054605.

[54] H. Fuchs, K. Mohring, Rep. Progr. Phys. 57 (1994) 231.

[55] A. Keksis, et al., Phys. Rev. C 81 (2010) 054602.

[56] I. Lombardo, et al., Nuclear Phys. A 834 (2010) 458c–460c.

[57] W. Bauer, C.K. Gelbke, S. Pratt, Ann. Rev. Nucl. Part. Sci. 42 (1992) 77–100.

[58] G. Verde, A. Chbihi, R. Ghetti, J. Helgesson, Eur. Phys. J. A 30 (2006) 81–108.

[59] L.W. Chen, V. Greco, C.M. Ko, B.A. Li, Phys. Rev. Lett. 90 (2003) 162701.

[60] L.W. Chen, C.M. Ko, B.A. Li, Phys. Rev. C 69 (2004) 054606.

[61] D. Dell'Aquila, Phys. Rev. Lett. 119 (2017) 132501.

[62] D. Dell'Aquila, et al., Investigation of the Hoyle state in ^{12}C with a newhodoscope detector, J. Phys. Conf. Ser. 876 (1) (2017) 012006. http://dx.doi.org/10.1088/1742-6596/876/1/012006.